Bubble impact on a tilted wall: Removing bacteria using bubbles

Ehsan Esmaili,[1,3] Pranav Shukla,[1] Joseph D. Eifert,[2] and Sunghwan Jung[1,3,*]
[1]*Department of Biomedical Engineering and Mechanics, Virginia Tech, Blacksburg, Virginia 24061, USA*
[2]*Department of Food Science and Technology, Virginia Tech, Blacksburg, Virginia 24061, USA*
[3]*Department of Biological and Environmental Engineering, Cornell University, Ithaca, New York 14853, USA*

(Received 17 May 2018; published 29 April 2019)

Dynamics of a bubble impacting and sliding on a tilted surface has been investigated through experimental and computational methods. In experiments, bubble-wall interaction has been characterized with an air bubble of about 550 μm in radius and a rising speed of about 30 cm/s as it impacts a solid substrate of a wall angle between 0° and 40°. Specifically, shear stress generated on the wall has been calculated and compared with bacterium adhesion force in order to evaluate a potential sanitization function. We numerically solved a force balance including buoyancy, hydrodynamic inertia and drag, and lift and thin film force to determine the bubble motion. Results showed that the shear stress increases with the wall inclination. The maximum shear stress goes up to more than 300 Pa as a single bubble impacts and scrubs a tilted wall. We found that such a high shear stress is attributed to a rapid change in thin film curvature (flipping bubble-water interface) during the bouncing stage. Later, during the sliding stage, a smaller shear stress up to around 45 Pa is generated for a longer period. We also showed that the shear stress generated during the bouncing and sliding stages is high enough to remove bacteria from a surface as a potential method for removing bacteria from tilted surfaces.

DOI: 10.1103/PhysRevFluids.4.043603

I. INTRODUCTION

The cleaning mechanism of using bubbles for wastewater treatments or microorganism removal has been proven as a sustainable and environmentally benign method in many industrial applications [1–5]. From a mechanics point of view, the force of a bubble impacting and sliding on a wall plays an important role in removing biofilms and dirt from various surfaces [6–9]. Recently, it has been shown that a continuous stream of single bubbles, with shear stress on the order of ∼0.01 Pa, can prevent biofouling growth [10]. Another new application of using the bubble-cleaning method is to clean agricultural produce like fruits and vegetables, which has yet to be studied extensively. Recently, cleaning foodborne pathogens on fruits and vegetables has drawn much attention due to food poisoning of millions of people every year [11–13]. Bubbles could be used to clean fruits and vegetables while also keeping them fresh with the gentle rubbing action from the bubbles and a minimal use of chlorine [14]. As chlorinated solutions are known to be carcinogenic and biohazardous [15–17], the use of bubbles for produce cleaning is a better alternative.

Understanding the dynamics of a bubble interacting with a solid surface is very important in order to control the removal of microcontaminants from the surface. Practically, there are two bubble-generation methods used: bubble-cavitation and bubble-injection methods. In general, cavitated bubbles collapse and create liquid jets toward a solid surface, which produce enormous shear stress to kill and remove cells from the surface [18,19]. However, this method can damage

*sunnyjsh@cornell.edu

soft surfaces and increase the temperature of a liquid bath rapidly, which can elevate the bacteria concentration in a liquid bulk. Another way to create bubbles is to inject pressurized air in water, which does not increase the bulk temperature. Once bubbles are injected at the bottom of the tank, the bubbles will then rise, impact, and scrub contaminated surfaces by impacting or sliding along the surface. Also, the injected bubbles last longer compare to bubble-cavitation cases, which can result in a longer cleaning time.

The shape, velocity, and path of a freely rising bubble have been investigated by many researchers [20–24]. Generally, the bubble shape can be categorized into three regimes of spherical, ellipsoidal, and spherical-cap bubbles as a function of the Reynolds, Bond, and Morton numbers [20]. Due to our focus on small bubbles of a radius less than 1 mm, we consider only either spherical or slightly ellipsoidal shaped bubbles. In terms of the interfacial mobility, the bubble dynamics can be classified into two cases of mobile (or fast bubble) and immobile bubbles (or slow bubbles) [25,26]. If a bubble-liquid interface is contaminated by particulates or surfactants, the interface holds a condition of zero tangential velocity. It is referred to as an immobile bubble, which reaches a slow terminal rising velocity. For a mobile bubble case (or fast bubble), the liquid-bubble interface can have nonzero tangential velocity because of low contamination. Hence, a condition of zero tangential shear stress is applied, and as a consequence, a mobile bubble achieves a higher terminal velocity [26]. From a practical point of view, bubbles in tap water are observed to be both mobile and immobile bubbles [23,25]. As a bubble approaches the wall, a thin liquid-film forms between the bubble and the substrate and the surface wettability does not change the bubble dynamics as long as a thin film exists [27]. Previous research on a thin film between a bubble and a wall has shown that the stability of a thin film strongly depends on the mobility of the bubble-liquid interface [28], the surface roughness [29], or even oscillations of the wall [27].

Most previous experiments or simulations have been performed only with horizontal surfaces [26,30–32] except for only a handful of articles for tilted walls to the best of our knowledge [33–37]. Studies for spherical-cap bubbles [33] and spherical bubbles [34] showed different bouncing and sliding behaviors of a bubble on a tilted wall. However, these previous studies focused on experimental observations and used scaling arguments rather than solving coupled macroscopic and microscopic equations. Furthermore, a lift force is not considered, which is important for understanding the bubble bouncing behavior. Later, Podvin *et al.* [35] used a lubrication theory to describe a thin film layer formed between an immobile bubble and a tilted wall without taking into account a lift force. There have been some two-dimensional numerical simulations investigating the effect of the Reynolds number, Bond number, and a wall angle [36,37]. But no detailed description or explanation of a thin film profile was reported in these studies. In addition to the bouncing stage, many studies have been dedicated to the sliding motion of the bubble in which the normal component of velocity goes to zero and the bubble slides along the wall due to buoyancy force. In fact, the dynamics and asymmetric shape of a thin film might play a key role in sliding dynamics according to many studies of a similar effect of an asymmetric shape of a bubble or a droplet on its motion in a Hele-Shaw cell [38,39], on a tube wall [40], and over a solid wall [41–43]. In summary, the effect of an asymmetric thin film and lift force on an impacting three-dimensional bubble can be crucial in understanding bubble-wall interactions.

To remove any substance including biofilms from a wall, scrubbing action with shear force is required. The magnitude of shear force to remove biofilms strongly depends on the physical and chemical properties of the wall surface and attached bacteria [44–47]. For example, in a laminar flow without the presence of bubbles, *Escherichia coli* needs a shear stress of $0.03 - 5$ (Pa) to get detached from hydrophobic substrates [45], while this shear stress varies in the range of 24–144 (Pa) for removing *Listeria monocytogenes* from a stainless steel surface [48]. But in case of having the bubbles in fluid flow, Sharma *et al.* [7] reported that the presence of microbubbles in the channel increases the detachment rate of *A. naeslundii* bacteria from 40% to 98% [7]. This is in line with recent study in bubble-induced detachment, which shows air bubbles inside the channel can increase the detachment of a *Staphylococcus aureus* strain up to 80% [49]. Furthermore, it has recently been shown that the mechanical stress of fluid flow can be an important factor in forming a biofilm and

act as a trigger for biofilm development [50]. Hence, shear flow induced by bubbles near the wall can play a key role in forming biofilms and cleaning of microcontaminants from the solid substrate.

In summary, most of the previous studies on bubble dynamics have focused on the impact of a bubble on the horizontal wall. To our knowledge, very little attention has been given to numerical simulation and modeling of the shear force generation of mobile bubbles on inclined solid walls. Hence, in the present study, we investigate the dynamics of a bubble interacting with an inclined surface at various angles. Section II describes the experimental setup used to generate a bubble and observe its interaction with a solid glass substrate at different angles. We numerically compute the dynamics of a bubble impacting a tilted surface using force balances as described in Sec. III. First, we numerically solve the governing equation of a thin liquid layer between bubble and wall and compare the results with our experiments. The following Sec. IV compares the experimental and numerical simulation results. We also discuss the application of a bubble impacting by calculating the shear stress generated by the bubble on the wall surface. Our conclusion will be discussed in Sec. V by comparing generated shear stress with minimum shear stress required to clean bacteria from the surfaces.

II. EXPERIMENT SETUP

A. Bubble-impact chamber

We designed an experimental setup to study the dynamics of bubble-wall impact. An acrylic container with a dimension of $10 \times 10 \times 12$ cm was filled with distilled water. Then we fixed a glass microscope slide after it was cleaned using ethanol (70%) solution, as shown in Fig. 1. To study the effect of a bubble-impact angle, we changed the inclination of the glass plate from 0° to 42°. A glass needle with a diameter of approximately 50 μm was used to generate a single bubble, which was manufactured using a Flaming/Brown Micro-pipette puller (Sutter Instrument P-1000). A controlled flow was used to inject air to generate bubbles using a syringe pump (NE-1000 Programmable Single Syringe Pump). The radius of the injected bubbles was about $R \approx 520$–550 μm. The motion of a bubble was recorded at 4000 frames/sec using a high-speed camera (Edgertronic SC2+). Figure 1(a) shows a schematic of the experimental setup used with a rising bubble.

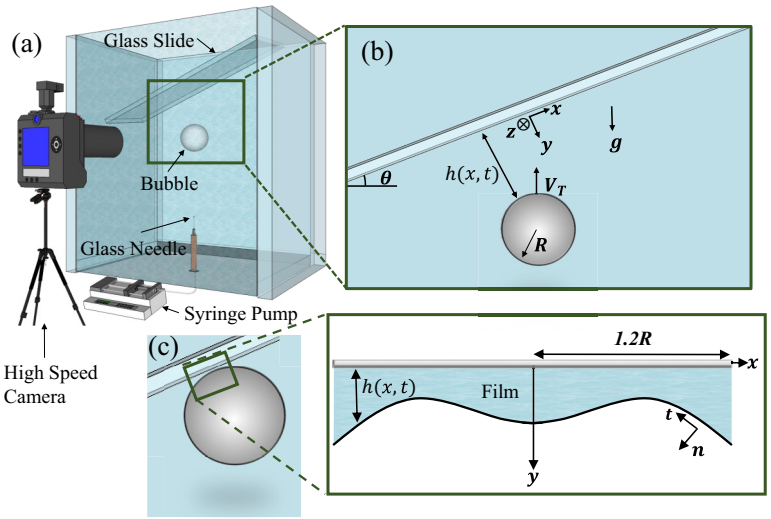

FIG. 1. (a) Large-scale schematic of a bubble rising and impacting a tilted surface; (b) zoom-in schematic of a bubble impacting a substrate with a coordinate system; (c) a liquid film between a bubble and a wall is squeezed and deformed due to the bubble impact.

For each experimental condition, five repeated trials were conducted to check the statistical significance of results. A rising bubble accelerates from the rest position at the tip of the needle and rises toward the wall while it reaches a terminal velocity before its impact with the wall. During the rising stage, the Reynolds number $\mathrm{Re} = 2\rho RV/\mu$ was found to be approximately 300 in our experiment, where ρ is the water density, R is the bubble radius, V is the bubble velocity, and μ is water viscosity. Also when a bubble slides along a tilted wall, the Reynolds number can change in the range 40–120 depending on the tilt angle. Moreover, during the rise, the Bond number ($\mathrm{Bo} = \Delta\rho g R^2/\sigma$), the Weber number ($\mathrm{We} = \rho V^2 2R/\sigma$), and the Morton number ($\mathrm{Mo} = g\,\mu^4\Delta\rho/\rho^2\sigma^3$) were measured to be 3.3–3.7 $\times\ 10^{-2}$, 1.2–1.3, and 2.62 $\times\ 10^{-11}$, respectively.

B. Particle image velocimetry

A similar setup was used to conduct particle image velocimetry (PIV) tests for capturing a vorticity structure around the bubble. But the box size was reduced to a smaller one (5 $\times$ 1 $\times$ 8 cm) to make sure that we can have enough particles in the plane of a bubble movement. For flow visualization around a bubble, 10 μm diameter hollow glass spheres (Dantec Dynamics 80 A6011) were used, the same as in [51]. The bubble($R \approx 550\ \mu$m) is released from the glass needle (a diameter of approximately 50 μm). A halogen lamp (Lowel Pro-light) was placed as a backlight to capture the particles' movement. Also, image sequences were recorded by a Photon camera (FASTCAM Mini UX) at 4000 frames/sec, and the PIVlab software [52] was used to track the particle motions around the bubble. The multipass, multigrid window deformation technique with two passes and Gaussian subpixel fitting have been used, ensuring enough particles were in the initial pass (64×64 pixels) [51]. Here, by assuming a continuous liquid phase inside the bubble, we estimated the imaginary point vortex (ω_z) at the bubble center from the circulation [$\Gamma(t)$] around the bubble. Specifically, the vorticity, ω_z, was calculated from the tangential velocity, u_s, using the relation $\Gamma(t) = \int_0^{2\pi R} u_s\, ds = \omega_z \pi R^2$. Here s is a coordinate along a closed circle and u_s is the tangential velocity along the curve. To implement the vorticity in our numerical model, we assume that vorticity follows a Gaussian distribution as $\omega_z = \omega_0 \exp[-(t - t_c)^2/C]$ where ω_0, t_c, and C are parameters obtained from PIV experiments.

III. THEORY

To describe the dynamics of a bubble near the tilted wall, all fluid forces that act on the bubble should be taken into account. Buoyancy force drives a bubble toward the wall due to gravity and a density difference. Drag force always acts in the opposite direction of the bubble movement, which originates from pressure gradient or viscous resistance in the liquid. Also, we take into account an added mass as a result of either accelerating or decelerating motions of the surrounding fluid. As a bubble impacts and squeezes a liquid film between the bubble and the wall, the thin liquid layer exerts resisting force against the bubble [26]. A history force takes into account the effect of vorticity diffusion around a bubble as it changes its velocity [53]. In the previous studies, it was shown that the order of magnitude of the history force in clean bubbles (mobile interface) is smaller than that in contaminated bubbles (immobile interface) or solid spheres [54,55]. So we can assume that the history force on a clean bubble at finite Re is negligible as assumed in other similar studies [26,56]. In this study, we modeled and emphasized the effect of lift force around a bouncing bubble. Lift force has been discussed in many cases of the rising bubbles along a vertical wall [57,58]. However, to our best knowledge, the effect of lift force on a bubble bouncing a tilted wall has not been studied. In this section, we will go over all these forces in detail.

A. Buoyancy force

A bubble rises toward the wall due to the buoyancy force, which depends on the gravity and the density difference between air and water. The buoyancy force on the bubble can be

expressed as

$$F_B^{(x)} = \rho g \Omega \sin(\theta)\, \hat{e}_x, \tag{1}$$

$$F_B^{(y)} = -\rho g \Omega \cos(\theta)\, \hat{e}_y, \tag{2}$$

where $\Omega = \frac{4}{3}\pi R^3$ is the bubble volume and $\hat{e}_x$ and $\hat{e}_y$ are the parallel and normal components of a wall coordinate system depicted in Fig. 1(b).

B. Drag force

There have been many studies investigating drag force depending on many factors such as the interfacial mobility, the Reynolds number, and the distance to the wall [26,57–61]. To determine the surface mobility of a bubble, we measured the terminal velocity of the freely rising bubble in our experiments, which is on the order of $V_T \approx 29$–30 cm/s. This is in a good agreement with reported studies for a mobile bubble rising in water [26,32]. Hence our bubble can be assumed to have a mobile bubble-water interface condition.

For the mobile bubble at high Reynolds numbers with a finite distance to the wall, the drag coefficient can be obtained assuming a potential flow as [59,62]

$$C_D^{(x)}(b) = \frac{48}{\mathrm{Re}}\left[-1 + \frac{1}{2}\left(\frac{1}{2b}\right)^3\right]^{-2}, \tag{3}$$

$$C_D^{(y)}(b) = \frac{48}{\mathrm{Re}}\left[-1 + \left(\frac{1}{2b}\right)^3\right]^{-2}, \tag{4}$$

where the normalized stand-off distance is $b = (H + R)/R$ and H is the distance between a bubble surface and the wall. Then the drag force can be determined as

$$F_D^{(x)} = -\frac{\pi}{4} C_D^{(x)}(b)\,\mathrm{Re}\ \mu R U\, \hat{e}_x, \tag{5}$$

$$F_D^{(y)} = +\frac{\pi}{4} C_D^{(y)}(b)\,\mathrm{Re}\ \mu R V\, \hat{e}_y. \tag{6}$$

C. Thin film force

A thin layer of a liquid is formed between a bubble and the wall as shown in Fig. 1. The film thickness, h, is on the order of a few micrometers. If the thickness goes down to the nanometer scale, it can lead to a thin-film rupturing event onto the wall [63,64]. However, based on Ref. [26], a liquid thickness remains on the order of micrometers during the bouncing stage, and a stable liquid film plays a crucial role in the motion of the bubble. To obtain a pressure distribution on a bubble-water interface, the normal stress, T, is balanced with the surface tension, σ, as [65] $T \cdot n = \sigma \nabla \cdot \hat{n}\,\hat{n} + \frac{\partial \sigma}{\partial s}\hat{t}$, where $\hat{n}$ and $\hat{t}$ are the normal and tangential unit vectors to the interface, respectively. The normal vector $\hat{n}$ can be expressed as $\hat{n} = -\frac{\partial h}{\partial x}\hat{e}_x + \hat{e}_y - \frac{\partial h}{\partial z}\hat{e}_z$. With a small-slope assumption of $|\nabla h| \ll 1$, the curvature $(\nabla \cdot \hat{n})$ can be approximated as $-\nabla^2 h$. Hence, the pressure difference inside a thin film becomes [35]

$$P_f = \frac{2\sigma}{R} - \sigma\left(\frac{\partial^2 h}{\partial x^2} + \frac{\partial^2 h}{\partial z^2}\right). \tag{7}$$

Here we assume that thin film dynamics are governed by a lubrication approximation (i.e., the Stokes-Reynolds equation). Then we calculate the thickness profile of a thin film as [66]

$$\frac{\partial h}{\partial t} = U\frac{\partial h}{\partial x} + \frac{1}{3\mu}\frac{\partial}{\partial x}\left(\frac{\partial P_f}{\partial x}h^3\right) + \frac{1}{3\mu}\frac{\partial}{\partial z}\left(\frac{\partial P_f}{\partial z}h^3\right), \tag{8}$$

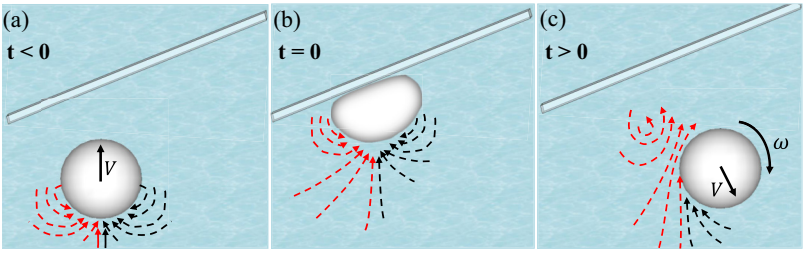

FIG. 2. A reminiscent wake flow behind a rising bubble makes the bubble rotate during the bouncing stage.

where $U = V_T \sin(\theta)$. We can solve Eqs. (7) and (8) simultaneously using appropriate boundary conditions [$P_f = 0$ and $dh/dt = -V = -V_T \cos(\theta)$ at $x = \pm 1.2R$ and $z = \pm 1.2R$ as shown in Fig. 1(c)]. Consequently, by having the pressure distribution and thickness of a thin film, the force of a thin film onto a bubble can be obtained by

$$F_F^{(x)} = \iint_A (P_f \cdot n_x)\, dx\, dz\, \hat{e}_x = -\iint_A P_f \frac{dh}{dx}\, dx\, dz\, \hat{e}_x, \tag{9}$$

$$F_F^{(y)} = \iint_A (P_f \cdot n_y)\, dx\, dz\, \hat{e}_y = \iint_A P_f\, dx\, dz\, \hat{e}_y. \tag{10}$$

D. Added mass force near a wall

Next, the added-mass terms are considered since a bubble moves unsteadily near the wall. Added-mass coefficients are $C_m^{\parallel}$ (parallel to the wall) and $C_m^{\perp}$ (perpendicular to the wall). Then the inertia force of a rigid bubble becomes as reported in Ref. [67]

$$\begin{aligned} F_I^{(x)} &= -\frac{d(\rho\, C_m^{\parallel} \Omega U)}{dt}\, \hat{e}_x, \\ F_I^{(y)} &= \frac{d(\rho\, C_m^{\perp} \Omega V)}{dt} \hat{e}_y + \frac{1}{2}\left[\frac{d(\rho\, C_m^{\parallel} \Omega)}{dH} U^2 + \frac{d(\rho\, C_m^{\perp} \Omega)}{dH} V^2\right] \hat{e}_y. \end{aligned} \tag{11}$$

Here $C_m^{\parallel}$ and $C_m^{\perp}$ depend on the bubble shape or the stand-off distance [31,59,67,68]. We will use the added mass coefficients depending on the bubble shape as $C_m^{\parallel} = C_m^{\perp} = C_m = 0.62\chi - 0.12$ [31]. We use χ as the ratio of the major to minor lengths of a rising bubble that is defined as $\chi = (1 - 1.17\lambda + 2.74\lambda^2)/(0.74 + 0.45\lambda)$, where $\lambda = R/R_0$ and R_0 is chosen to be 1 mm [26]. We will also study changes in the added mass coefficients, depending on the distance from the wall as [68]

$$\begin{aligned} C_m^{\perp} &= 0.5 + 0.19222\, b^{-3.019} + 0.06214\, b^{-8.331} + 0.0348\, b^{-24.65} + 0.0139\, b^{-120.7}, \\ C_m^{\parallel} &= 0.5 + 0.09608\, b^{-3.02} + 0.0194\, b^{-9.6} + 0.00546\, b^{-40.2}, \end{aligned} \tag{12}$$

where the normalized stand-off distance $b = (R + H)/R$.

E. Lift force

When a bubble rises, a wake is created behind and follows the bubble. Shortly after the bubble bounces off from a wall, the bubble is pushed in an angle depending on the wall orientation. Then the reminiscent rising wake keeps flowing around the bubble and generates a shear flow as illustrated in Fig. 2. Consequently the flow field around the bubble would produce a lift force which can make the bubble migrate laterally in the x direction.

To estimate the lift force, the effect of vorticity, $\vec{\omega}$, is taken into account as [69]

$$\vec{F}_L = C_L\, \rho \Omega\, \vec{\omega} \times \vec{V}, \tag{13}$$

where the bubble velocity is $\vec{V} = (U, -V, 0)$, the fluid vorticity at the center of the bubble is $\vec{\omega} = (0, 0, \omega_z)$, and C_L is the lift force coefficient. Previous studies addressed how a lift force of a bubble depends on various parameters such as an interfacial mobility, the vortex structure, the Reynolds number, and the bubble-wall distance [57,58,69–72]. Even though to our best knowledge there are no analytical expressions available for C_L of a clean bubble impacting the wall at moderate Reynolds numbers, we found that C_L for a clean bubble in a shear flow can range from 0.3 to 0.75 [69,71]. With the range of our conditions (Re = 50–140, maximum impact deformation = 1.12 R and $\chi \sim 1.5$), it has been shown that a lift coefficient can be considered as a constant [71,72]. Hence, it is reasonable to assume a constant lift coefficient for clean bubbles in our study. The lift force in the x and y directions will be

$$F_L^{(x)} = C_L\,\rho\Omega V\,\omega_z\,\hat{e}_x, \quad F_L^{(y)} = C_L\,\rho\Omega U\,\omega_z\,\hat{e}_y, \tag{14}$$

where V is positive when a bubble is moving towards the wall.

F. Force balance

By combining all forces described above (i.e., buoyancy, hydrodynamic drag, inertia with the added mass, film pressure, and lift force) in the x and y directions, we can get governing equations as

$$\rho\Omega\left[C_{m\parallel}\frac{dU}{dt} - \frac{d(C_{m\parallel})}{dH}VU\right] = \rho g\Omega\sin(\theta) - \frac{\pi}{4}C_D^{(x)}\,\mathrm{Re}\;\mu\,RU - \iint_A P_f\frac{dh}{dx}\,dx\,dz + C_L\rho\Omega V\omega_z, \tag{15}$$

$$\rho\Omega\left\{C_{m\perp}\frac{dV}{dt} + \frac{1}{2}\left[-\frac{d(C_{m\perp})}{dH}V^2 + \frac{d(C_{m\parallel})}{dH}U^2\right]\right\} = \rho g\Omega\cos(\theta) - \frac{\pi}{4}C_D^{(y)}\,\mathrm{Re}\;\mu\,RV - \iint_A P_f\,dx\,dz - C_L\rho\Omega U\omega_z. \tag{16}$$

To calculate U and V of a bubble's centroid, we need to solve two differential equations (15) and (16) numerically. In addition to the two unknowns U and V, the pressure inside a thin film, p, should be numerically computed. The thin film pressure and the bubble velocities are coupled through Eqs. (7) and (8). Similar to the previous work, a square computational domain has been used to represent a thin film area between a bubble and the wall [35], where a half of the domain size is $1.2R$. Since the maximum half-width of a deformed bubble is larger than its original radius, we chose the computation domain of $1.2R$ throughout simulations. The domain is divided into $N \times N$ nodes, and Eqs. (7) and (8) are discretized using a finite difference method. An initial condition for a thin film to solve Eq. (8) is assumed to be a parabolic distribution as $h_0(x, z) = H_0 + (x^2 + z^2)/(2R)$ where H_0 is an initial distance between the bubble surface and the wall. Also, on the outer boundary at $x = \pm 1.2R$ and $z = \pm 1.2R$, thin film pressure goes to zero, $P_f = 0$, and the film thinning rate is assumed to be the normal speed of a bubble, $\partial h/dt = -V$. Hence, $N \times N$ nodes in addition to Eqs. (15) and (16) were solved using a MATLAB ode15s solver. A similar numerical method has been reported previously [26,31,35,73]. Also, the mesh independency has been tested, which results in no significant change in the bubble motion for the following number of nodes: 75×75, 105×105, 135×135. In this study, $N = 105 \times 105$ has been used to calculate the bubble velocity profile except for Sec. IV D, where we increase the number of nodes to $N = 135 \times 135$ to a better resolution in calculating the shear stress on the wall.

It is also worth mentioning that the current method of using both the lubrication approximation for a thin film and the potential theory for a bubble motion has been investigated by many other researchers, showing good agreement between computational results and experimental observations [26,31,35]. This current method will ensure to have all the forces to be continuously computed to

simulate a bubble motion over an entire course of time without any discontinuity. The minimum Reynolds number is about 50 even when a bubble has zero normal velocity. But the Reynolds number stays around a few hundred most of the time, which ensures the validity of the potential theory. For the lubrication approximation, when a bubble is away from the wall, this approximation is not valid theoretically. However, the film force based on the lubrication approximation is close to zero while a bubble is away as shown below in Fig. 9. Hence, the final bubble kinematics will not be affected even though we keep the lubrication approximation over the entire time.

G. Numerical methods

To understand and characterize the bubble-wall interaction with a tilted wall, force balance equations shown in Eqs. (15) and (16) are solved numerically. We perform three different simulations to study the effect of lift force and different added mass coefficients and compared them with experiments. In the first model, we neglect the lift force and consider only added mass coefficients depending on the bubble shape ($C_m = 0.62\chi - 0.12$). Before bouncing, the shape parameter, χ, is calculated as described in Sec. III D. But after the first impact, we assume the bubble is almost spherical i.e., $\chi = 1$ [26] and $C_m = 0.5$. The second model considers the added mass coefficients of a sphere depending on the wall distance [Eq. (12)], while we still do not consider the lift force effect. For the third model, we include the lift force just between the first to second impact [Eq. (14)], while the added mass coefficients depend on the bubble shape ($C_m = 0.62\chi - 0.12,\ \chi = 1$). In the above three models, we set an initial distance to the wall to be 3.3 mm and assume that the bubble has already reached to its terminal velocity of $V_T \approx 30$ cm/s.

IV. RESULTS

A. Parallel and normal velocity of a bubble

Figure 3(a) shows different image sequences of a bubble interacting with the solid wall at an angle of 18°. A dotted blue line indicates the trajectory of a bubble centroid from $t = -3.5$ ms to 55.5 ms. At the time of $t = -3.5$ ms, the bubble has already reached its terminal velocity of

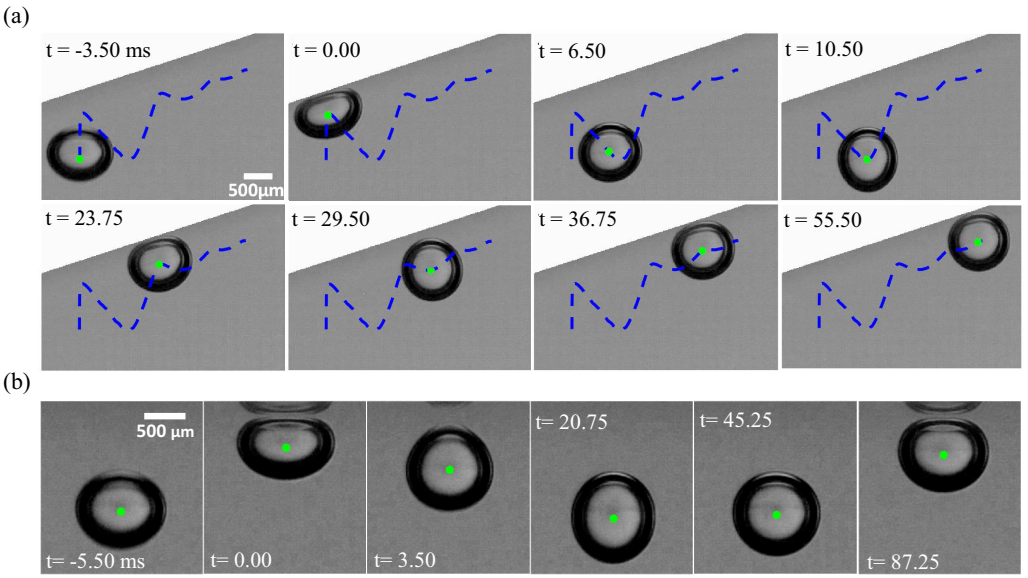

FIG. 3. A bubble impacting a wall. (a) A bouncing bubble from a tilted wall at 18°. The blue dotted line shows a trajectory of the bubble centroid, and the light green dot shows the centroid at a given time; (b) a bubble impacting a horizontal wall.

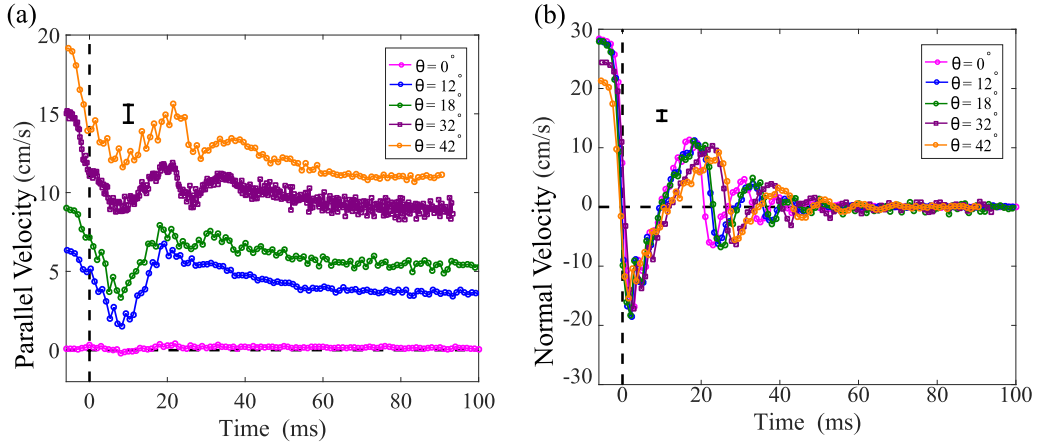

FIG. 4. Velocity profiles of a bubble with $R = 520$–$550\ \mu$m at five different tilted angles. (a) Parallel velocity, (b) normal velocity. The reference time is the impact time, and all velocity profiles are shifted to start at time 0. For each angle, an error bar is calculated by the root-mean-square deviation method for five trials over the time. Then average error bar of all angle is plotted at left corner.

$V_T \approx 30$ cm/s. After the bubble rises toward the wall, it impacts the surface at $t = 0$. As a result, a thin liquid film gets squeezed between the solid wall and the bubble, which results in increasing the pressure in the film. Such high thin film pressure pushes the bubble away from the solid wall, and the bubble bounces off. Therefore, the bubble accelerates, moves away from the wall, and reaches its maximum distance from the wall. When the bubble gets away from the wall, we can assume the thin film force and the wall effects are negligible and buoyancy force pushes the bubble back to the wall again. As the bubble approaches the wall, the normal velocity keeps descending, and the bubble impacts the surface for the second time at $t = 23.75$ ms. A similar bouncing process is repeated for three times or more. Later, as the bubble dissipates its kinetic energy, it slides along the wall.

To elucidate the effect of the wall angles, Fig. 4 shows the parallel and normal velocities of the bubbles (U and V) with a radius of $R \approx 520$–$550\ \mu$m for different inclinations of the wall. Here the error bar is estimated from the standard deviation of five trials on the same configuration. With an increase in the wall inclination, U velocity of the bubble increases, although V velocity slightly starts to decrease, showing more buoyancy force [$F_B^x \sim \rho g \Omega \sin(\theta)$] has been transferred to the x direction. Also, normal velocity profiles in Fig. 4(b) shows that the period between two impacts expands as the wall angles increases, mostly due to increasing of U velocity.

B. Numerical results

Figure 5 shows the comparison of three models with experimental velocity profiles for the case of the wall at an angle of $\theta = 18°$. Gray circles denote experimental results, and experimental error bars are shown in the left-top corner in black based on twice the standard deviation of five runs. The first and second models (pink and green lines) investigate the effect of added mass on the bubble dynamics, considering the higher order terms to added mass coefficient (green line) does not lead to accurate prediction for U velocity. Indeed, Eq. (12) has been derived for a sphere moving in ideal flow field [68] but might not be valid in our case due to rotational flows around the bubble. However, as shown in Fig. 5, the simulation including a lift force (the blue line) results in good agreement with the U velocity component compared to other models. This explains that when a bubble moves away from the wall, $V < 0$, the x component of the lift force in Eq. (14) acts as an extra drag on the bubble.

To obtain the bubble vorticity for applying in the third model (the blue line), we performed the PIV experiments as the bubble rises and impacts the wall at an angle of $\theta = 18°$. Figure 6 shows

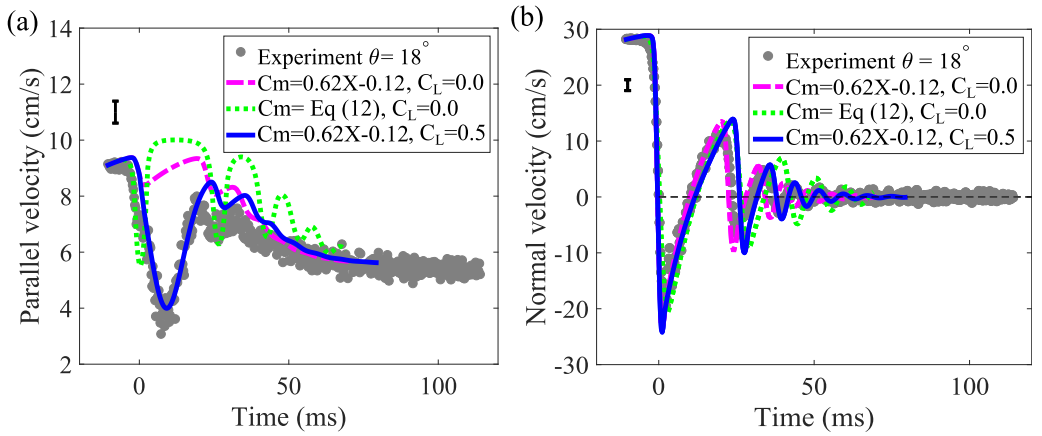

FIG. 5. (a) Parallel and (b) normal velocities of a bubble $R = 550\ \mu$m impacting a solid wall at an angle of $\theta = 18^\circ$. Gray circles are the averaged velocity of five experimental trials, and the corresponding error bar of twice the standard deviation is shown on the top-left corner in blue.

different snapshots of our PIV tests, revealing a strong clockwise rotation of particles inside the gap between the bubble and the wall as the bubble bounces off from the surface. In Fig. 7(a) the vorticity distribution around the bubble bouncing from the wall is shown. In Fig. 7(b) experimental results have been fitted with a Gaussian distribution, $\omega_z = \omega_0 \exp[-(t - t_c)^2/C]$, with the following parameters: $\omega_0 = 90.30\ \text{s}^{-1}$, $t_c = 9.07 \times 10^{-3}$ s, and $C = 6.16 \times 10^{-5}\ \text{s}^2$. We simulated our force model, Eqs. (15) and (16), with different C_L as shown in Fig. 8(a). $C_L = 0.5$ is in better agreement with our experiments than other C_L values (0.3 and 0.75). To check the sensitivity of our vorticity measurement, the parallel velocity of the bubble with $C_L = 0.5$ was plotted in Fig. 8(b) with 95% confidence intervals of the fitted vorticity.

C. Lift force on a bouncing bubble

To simply explain the numerical results in the previous section, we use a scaling argument to derive the order of magnitude of the lift force and its effect on the bubble dynamics. First, we

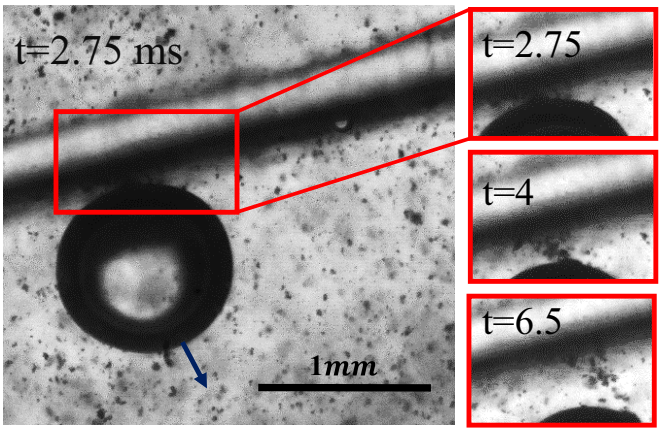

FIG. 6. Particles are scrubbed off from a wall by a bubble bouncing and rotating in the clockwise direction, $\theta = 18^\circ$.

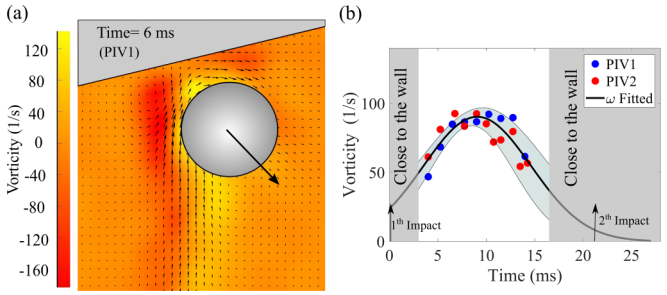

FIG. 7. (a) Vorticity structure around the bubble, obtained by a PIV test; (b) vorticity, $\omega_z(t)$, is calculated from the circulation around the bubble; two trials (PIV1 and PIV2) in the case of $\theta = 18^\circ$ and $R \approx 520$ μm. The vorticity is related to circulation as $\Gamma(t) = \omega_z(t)\pi R^2$ where circulation is measured around the bubble on different closed paths by $\Gamma(t) = \int u_s(t)\, ds$. Circles represent the average vorticity obtained by calculating the circulation along several closed paths with distances of $1.1R$ $1.2R$, and $1.3R$ from the bubble center. The black line is a fitted Gaussian distribution $[\omega_z = \omega_0 \exp(-(t - t_c)^2/C)]$, which is used in a lift force model. The best-fitted parameters are $\omega_0 = 90.30$ s^{-1}, $t_c = 9.07 \times 10^{-3}$ s, and $C = 6.16 \times 10^{-5}$ s^2 with 95% confidence intervals [83.78, 96.75] s^{-1}, $[8.50 \times 10^{-3},\ 9.63 \times 10^{-3}]$ s, and $[3.80 \times 10^{-5}, 8.52 \times 10^{-5}]$ s^2, respectively. Not enough data are available as the bubble gets close to the wall due to difficulty in tracking the particles in the gap between the bubble and the wall.

will estimate the order of magnitude of vorticity that is formed when a bubble bounces off. Then the interval between two impacts will be calculated, which roughly shows the timescale that the vorticity affects the bubble motion. Finally, by obtaining the magnitude of the generated vorticity and the timescale, the order of magnitude of the lift force and its effect on U velocity will be evolved.

1. Vorticity

As we explained in Sec. III E, a wake flow behind a rising bubble rotates around the bubble as it bounces away from the wall, and this can shape the vorticity structure around the bubble, leading to the lift force (Fig. 2). To approximate the velocity of flow behind the bubble, we use potential theory mainly due to high Reynolds number and the low aspect ratio during rising in our study ($\chi \sim 1.17$). However, it is worth noting that when a bubble deforms significantly (large aspect ratio

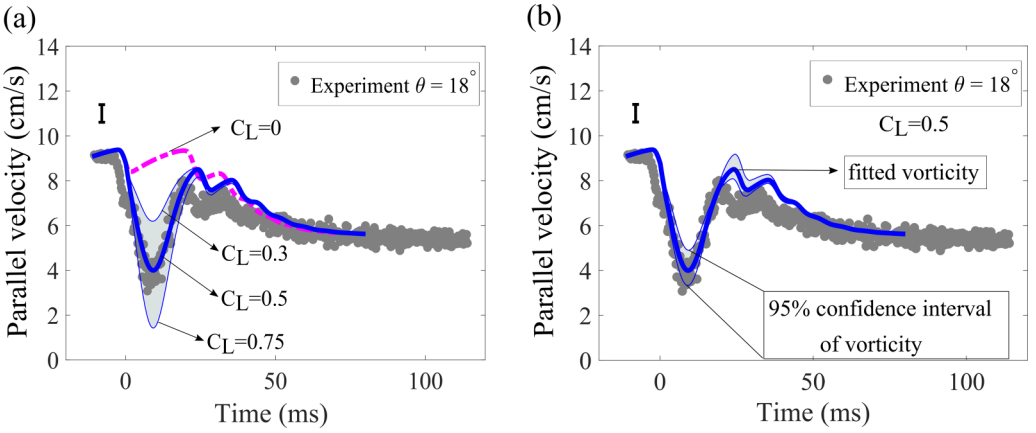

FIG. 8. (a) Parallel velocity of a bubble for several C_L values; (b) parallel velocity of the bubble ($C_L = 0.5$) with 95% confidence interval for vorticity fitting. The bubble (R = 550 μm) is impacting a solid wall at an angle of $\theta = 18^\circ$.

$\sim$2), the potential theory is not valid any longer [74] and the wake structure behind the bubble could lead to a helical or zigzag motion [75]. Based on the potential theory, for a sphere with constant velocity, V_T, the radial velocity component is derived as $u_r = \partial\phi/\partial r = V_T(R/r)^3\cos(\gamma)$ in which r is the distance from the bubble center and γ is the angle from the axis of symmetry. For the distance of $r \sim (2R - 3R)$ behind the bubble, the velocity scales as $u_r \sim (0.03\text{–}0.12)V_T$. Since this velocity rotates around the bubble during the bouncing stage, we can assume the tangential velocity around the bubble is on the same order of magnitude as the velocity in the wake flow behind the bubble ($u_s \sim u_r$). Now the circulation around the bubble can be calculated as $\Gamma = \int u_s\, ds$, which allows us to estimate the vorticity at the center of the bubble using the following relation: $\Gamma(t) = \omega_z \pi R^2 = \int u_s\, ds$. Consequently, the vorticity at the bubble center scales as $\omega_z \sim u_s/R$. In our study, for the terminal velocity of $V_T \approx 30$ cm/s and radius of $R \approx 550$ μm, the generated vorticity can be obtained as $\omega_z \sim (16\text{–}65)\ \mathrm{s}^{-1}$, on the same order of magnitude with PIV experiments [Fig. 7(b)].

2. *Frequency of bouncing*

Here we define the frequency of bouncing as an inverse of the period between two impacts. We divide it into two periods, $\Delta t \sim \Delta t_1 + \Delta t_2$. The Δt_1 corresponds to the time that a bubble is pushed back by thin film force while Δt_2 shows the later time when the effect of the thin film force vanishes and buoyancy and inertia forces form the bubble dynamics. During the Δt_1, the inertia and thin film forces are dominant [26], so we simply balance them in the y (normal-to-wall) direction and get

$$\rho C_m \Omega dV/dt \sim p\pi R^2. \tag{17}$$

By approximating the pressure as $p \sim \sigma/R$ and acceleration as $dV/dt \sim (V_r)/\Delta t_1$, where V_r is the maximum bubble velocity after bouncing, the following timescale is obtained: $\Delta t_1 \sim \rho C_m \Omega V_r/\pi\sigma R$ represents the timescale for the bubble to get to V_r from rest during the bouncing. If we choose the V_r to be on the order of the bubble terminal velocity ($V_r \approx V_T \approx 30$ cm/s), then Δt_1 is on the order of $\sim$(1–2) ms, which is much smaller than the bouncing period observed in experiments (roughly between 20 and 25 ms). It means that the thin film can affect the bubble only early during the bouncing. Then, for the later period Δt_2, the thin film force is negligible, and the bubble moves along the following path: the bubble starts to slow down from V_r as thin film force diminishes, and the buoyancy force acts against the bubble motion. Following that, the bubble velocity gets to zero at its maximum distance from the wall. Then the bubble changes its direction, and starts to get accelerated towards the wall again due to buoyancy force. It has to be mentioned that there is a short period before the bubble impacts the wall where a thin film force is dominant again. However, as we have shown before, it is on the order of Δt_1 and is smaller compared to the frequency of bouncing. Also, the drag force is negligible due to small bubble velocity over the period Δt_2. So balancing the inertia with the buoyancy force in the y direction, $[\rho C_m \Omega(2V_r)/\Delta t_2 \sim \rho g \Omega\cos\theta]$, shapes the dynamics of the bubble. As a result, the inverse of the bubble frequency can be obtained as $\Delta t \sim \Delta t_2 \sim 2C_m V_r/g\cos(\theta)$, which is about 30 ms close to experimental measurements (20–25 ms).

3. *Lift force effect*

In Fig. 5 we showed that including the lift force after the impact results in better prediction of U velocity of the bubble. Here we estimate the order of magnitude of the lift force in the x direction, explaining how U velocity is changed due to the vorticity formed during the impact ($\omega_z \sim u_s/R$) where $u_s \sim (0.03\text{–}0.12)V_T$. Based on Eq. (14), the lift force in the x direction ($C_L \rho\, \Omega V \omega_z$) can act as an extra drag when the bubble moves away from the wall, $V < 0$. We consider half of the bouncing time, $\Delta t_3 \sim \Delta t_2/2 \sim C_m V_r/g\cos(\theta)$, as a time that the bubble velocity is negative ($V < 0$) and the bubble is bouncing away from the wall. By balancing the inertia force with lift force in x direction $[\rho\Omega C_m dU/dt \sim \rho\Omega\, C_L \omega_z V_r/2$, $(V_r/2)$ is an average normal velocity since it varies linearly from V_r to 0], the following expression for velocity change can be derived: $\Delta U/\Delta t_3 \sim \alpha C_L/C_m V_r^2/2R$. Here ΔU is a change in velocity due to the effect of forming vorticity around the bubble. If we assume that the lift force and added mass coefficients are on the same order of magnitude ($C_L \sim C_m$), the radius

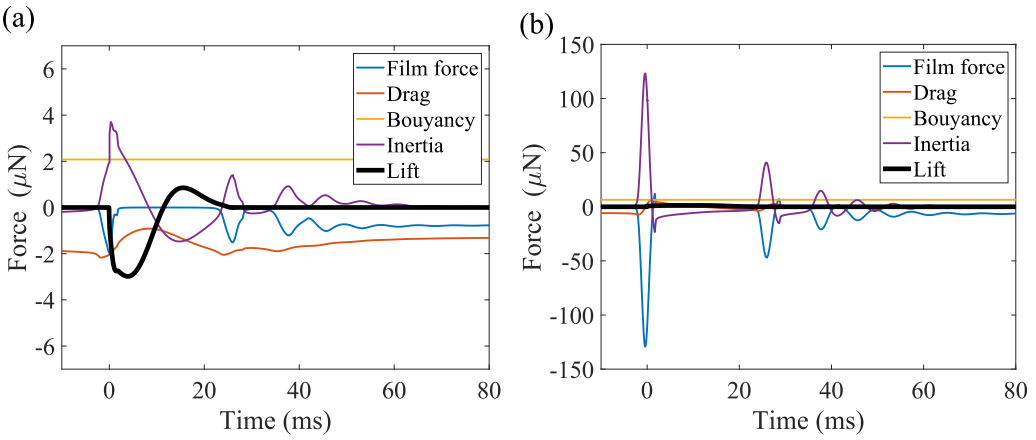

FIG. 9. Forces in x and y directions for the bubble at $\theta = 18^{\circ}$. The results are for the model with constant added $C_m = 0.62\chi - 0.12$ including lift force (blue line in Fig. 5). (a) Forces in the x direction; (b) forces in the y direction.

is about $R \approx 550\ \mu$m, $\alpha \sim (0.03\text{–}0.12)$, $V_r \approx 30$ cm/s, and $\theta \sim 18^{\circ}$, then ΔU can be estimated to be 4–15 cm/s, which is on the same order of magnitude as a change in U velocity during the first impact in Fig. 4(a).

Figure 5 shows the vorticity generated around the bubble plays a crucial role in the bubble velocity in the x direction. In the case of normal velocity, V, all three models are in good agreement with experiments, while in the x direction, the only model with lift force is accurate enough. It can be due to the order of lift force in the x and y directions. In fact, the ratio of lift force in the x and y directions can be defined as $F_y/F_x \sim U/V$, from Eq. (14), showing if U velocity is small during the bouncing compare to V, the lift force in the normal direction can be small, $F_y \sim F_x(U/V)$. More importantly, the order of magnitude of inertia, thin film, and buoyancy forces in the y direction are much bigger compared to the x direction (Fig. 9), making lift force even less important in the y direction. That is why the bubble dynamics is less affected by lift force in y direction, while it can play a key role in the x direction.

Figure 10 shows how a microscopic film between a bubble and a wall changes during the bubble interaction with the wall of $\theta = 18^{\circ}$. First, the pressure inside the liquid film slowly increases upon the impact. Then, the high-pressure region spreads out radially, and a bubble dimple is formed [76,77]. The dimple formation is a result of the faster drainage of a liquid near the edge of a film than that of a liquid at the center. As shown in Fig. 10, the asymmetric shape of a film is observed. While the bubble is approaching the wall during $t = -0.86$ ms to $t = 0$ ms, two dimples are formed at the left and right sides of the bubble, and minimum thickness occurs at the left side of the bubble. But as the bubble bounces during $t = 0$ to $t = 1.2$ ms, the film location with the minimum thickness shifts to the right side of the bubble. Such an asymmetrical profile can lead to the tangential thin film force introduced in Eq. (9) and an extra drag.

After several bounces, a bubble starts to slide along the wall as its normal velocity goes to zero (if $\theta < \theta_{\text{critical}} = 55^{\circ} \pm 5^{\circ}$) [34,35]. Here we briefly investigate the terminal velocity of mobile bubbles, sliding along a tilted wall at different angles. It has been shown that a sliding bubble experiences more drag compare to a freely rising bubble [34,60]. In the case of high Reynolds number bubbles, the overall drag coefficient of $C_D \approx 100/\text{Re}$ has been reported for $45 < \text{Re} < 200$ [34], approximately twice bigger than a freely rising bubble in unbounded liquid ($C_D \approx 48/\text{Re}$) [34]. It also has been shown that a viscous force of dynamic meniscus should be taken into account [41,42]. In Fig. 11 we compare the terminal sliding velocity of the bubbles with experimental values for different tilted angles, showing a good agreement between numerical and experimental

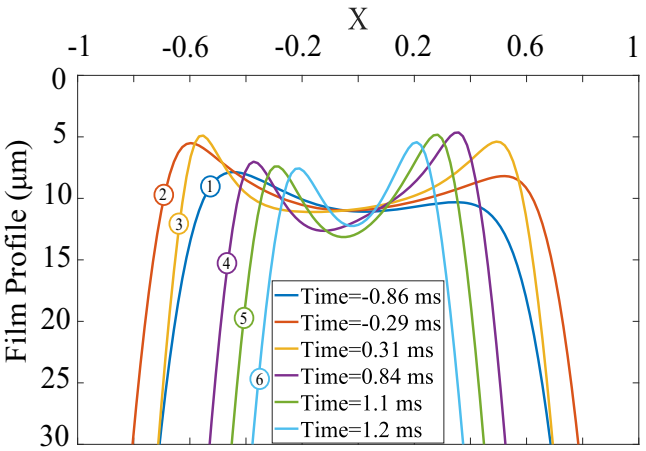

FIG. 10. Thin film profiles for a bubble with $R \approx 550$ μm during the impacting and bouncing stage at the wall angle of $\theta = 18^\circ$. X is normalized by the size of the domain.

velocities. In fact, in this study, a deformable bubble-liquid interface enables us to determine the asymmetric shape of the thin film, $h(x, z, t)$, and consequently the tangential thin film force ($\approx \iint_A P_f \frac{dh}{dx}\, dx\, dz$).

D. Shear force and shear rate

Fluid motions near a wall can generate normal and shear stresses at the surface, possibly enough to remove biofilm from the wall. In this section, we investigate the shear stress induced by an impacting bubble on the wall. When a bubble approaches a wall, a thin fluid layer between the bubble and the wall is squeezed out from the center. Later, when the bubble gets away from the wall, the fluid is sucked back in to fill the gap. Both squeezing and suction processes generate strong shear rate and stress on the wall as the bubble approaches and bounces away. Here we calculate the velocity profile inside the thin film in order to measure the generated shear stress on the wall. Based

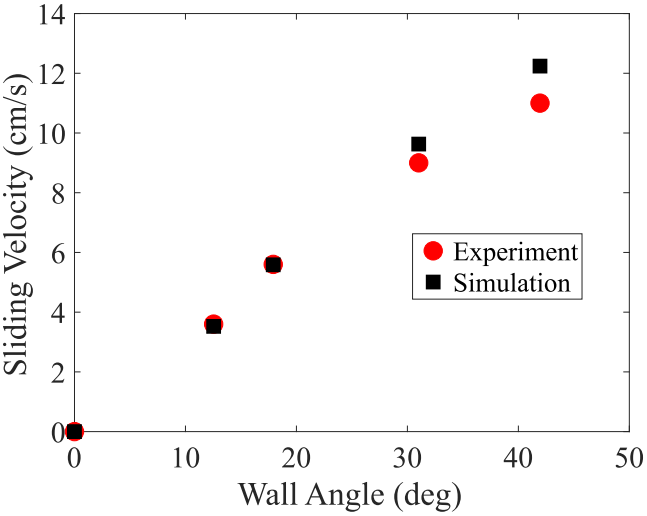

FIG. 11. Experimental and simulated sliding velocities of a bubble at different wall angles.

on our assumptions in Sec. III C, fluid velocities in x and z directions are hyperbolic as

$$v^{(x)} = \frac{1}{\mu}\frac{\partial P_f}{\partial x}\left(\frac{y^2}{2} - hy\right) - U, \tag{18}$$

$$v^{(z)} = \frac{1}{\mu}\frac{\partial P_f}{\partial z}\left(\frac{y^2}{2} - hy\right). \tag{19}$$

Here, with a lubrication approximation, we neglect the normal component of velocity, $v^{(y)} = 0$. Then the shear stresses on the wall can be derived as

$$\tau^{(xy)} = \mu\left(\frac{\partial v_x}{\partial y}\right)\Big|_{y=0} = -h\frac{\partial P_f}{\partial x}, \tag{20}$$

$$\tau^{(zy)} = \mu\left(\frac{\partial v_z}{\partial y}\right)\Big|_{y=0} = -h\frac{\partial P_f}{\partial z}. \tag{21}$$

Figure 12 shows how shear stress along the x direction (τ_{xy}) propagates as a bubble with radius $R \approx 520$ μm impacts and bounces away from the horizontal wall, $\theta = 0^\circ$. In Figs. 12(a) and 12(b), as the bubble moves toward the wall, we observe that the peak of shear rate radially propagate outward, as well as the position of a dimple [Fig. 12(c)]. But then it retreats back inside as the bubble bounces back [Figs. 12(e) and 12(g)]. To evaluate the order of magnitude of shear stresses generated during the bubble interaction with the wall, we plotted the maximum normal pressure and shear stress in the x direction, τ_{xy}, for two different wall inclinations, Figs. 13(a) and 13(b). To capture the high resolution of shear stress dynamics, we choose the time step of ($\Delta t = 1 \times 10^{-5}$ s) during the bouncing process. As shown in Fig. 13, for each approach-retract motion, two peaks in the pressure and shear stress have been formed. Two correspond to approach and retract moments, for example, the period of ($\sim -3 < t < 2$) in Fig. 13(a). The peaks can get to 210 Pa and will be explained latter by scaling arguments. Also, Fig. 14 shows that the maximum shear stress generated during both the first impact, and the sliding stage increases with the wall angle. For example, on the wall of $\theta = 42^\circ$, the shear stress reaches up to 307 Pa during the first impact and 44.5 Pa during the sliding stage.

Moreover, our study shows no significant effect of a lift force on the maximum and sliding shear stress. For example, in the case of the wall angle of 18° we found a less than 2% difference between the maximum shear stress with a lift force and the one without a lift force; the shear stress without a lift force, 211 Pa, is slightly higher than the one with the lift force, 209.6 Pa. Also, during the sliding stage, there is no rotational flow around a bubble, so the lift force does not affect the shear stress during the sliding stage either. Therefore, all cases in Fig. 14 have been simulated without a lift force due to the insignificant change by the lift force.

1. Scaling argument

Here we estimate shear stresses that can be generated during the bubble bouncing. Close to the impact moment at $t = 0$, the schematic is shown in Fig. 12(d), the capillary-driven surface deformation leads to the formation of two dimples. The dimple moves with v_d velocity, which can be defined as $v_d \sim \sqrt{\sigma/\rho R}$ (capillary wave speed with the wave number of R^{-1}) [78]. So we can scale the shear stress as $\tau \sim \mu v_d/h$. By considering a bubble impacting the horizontal wall, $R \approx 520$ and $h \sim$ (5–10) μm, shear stress of $\tau \sim$ (37–74) Pa will be obtained, which is of the same order of magnitude as the simulated value ($\tau \sim 30$ Pa) in Fig. 13(a) at $t = 0$.

By looking at the inset plot in Fig. 13(a), the second and sharper jump in shear stress emerges right after the bubble bounces away from the wall. At this stage, due to the rising motion of the bubble, the flow in the thin film is sucked toward the center, and two existing dimples start to move inward. As they reach the center of the bubble and merge, the curvature of liquid profile changes rapidly, pushes away the liquid, and generates larger shear stress on the wall [Fig. 12(h)]. We called

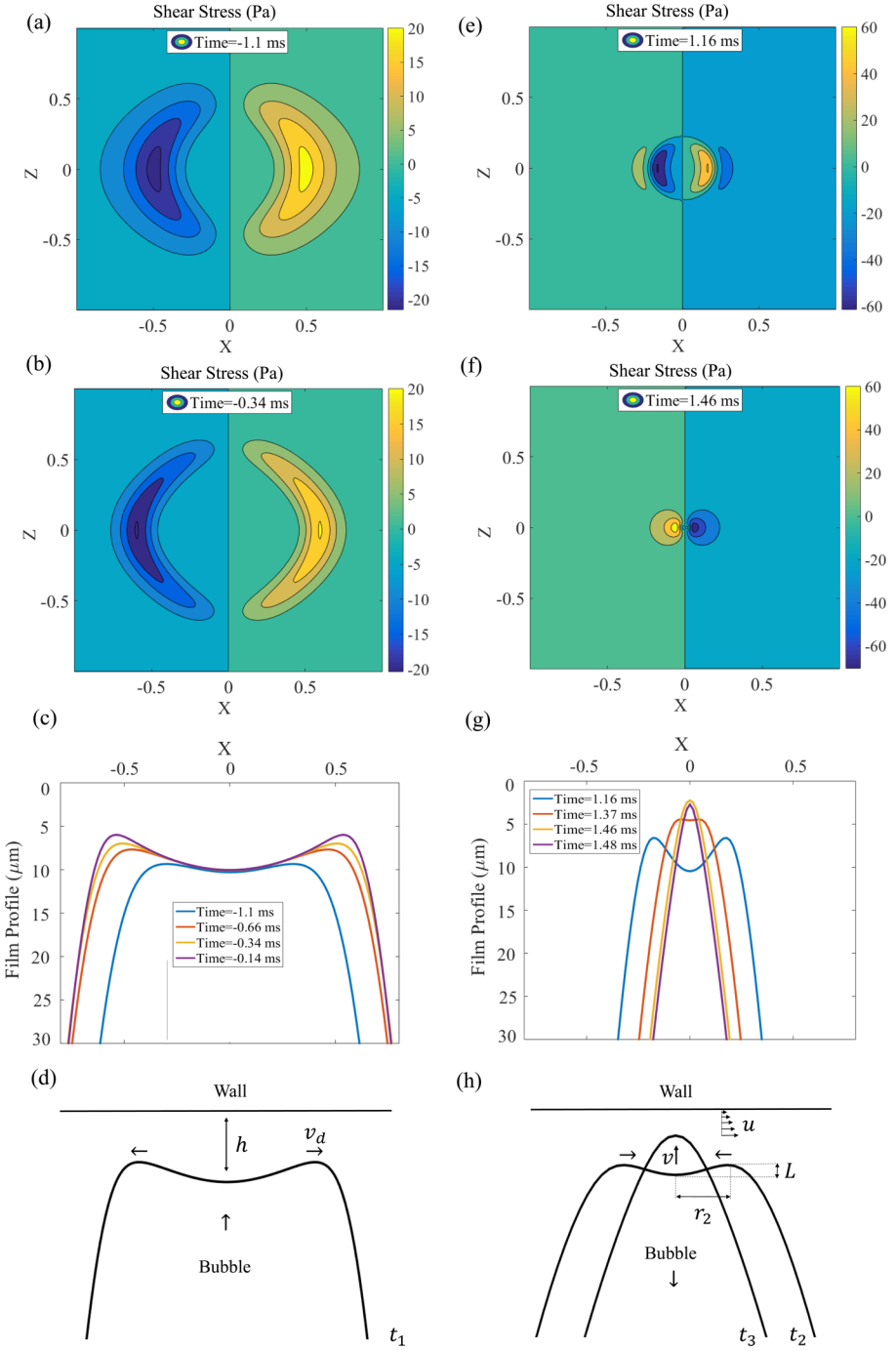

FIG. 12. Shear stress (τ_{xy}) propagation and thin film profiles for the bubble($R \approx 520$ μm) impacting a horizontal wall, $\theta = 0$. X and Z are normalized by the size of domain; (a)–(c) the shear stress formation and thin film profile as the bubble impacts the wall; (d) the schematic of the bubble approaching the wall and two dimples propagate toward the outside; (e)–(g) the bouncing stage; (h) the schematic of a thin film as its curvature changes during the bubble bouncing from the wall, and two incoming dimples merge and result in a rapid curvature change of the thin film, concave to convex profile from t_2 to t_3.

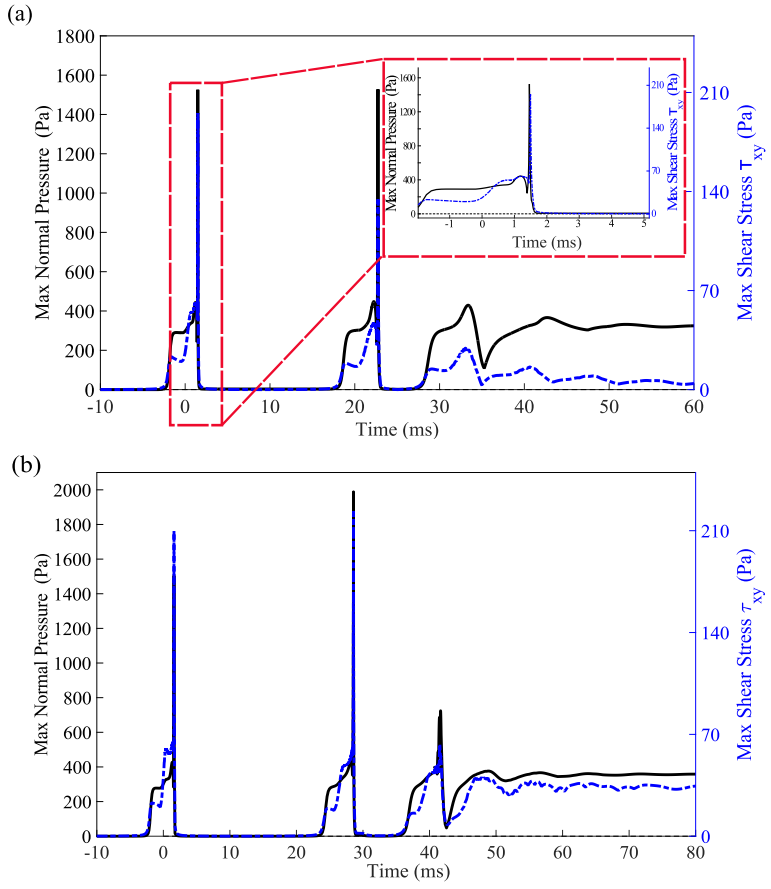

FIG. 13. Maximum normal and shear stress on a wall. (a) $R \approx 520$ μm impacts on a horizontal surface, $\theta = 0°$; (b) $R \approx 550$ μm impacts on a tilted surface, $\theta = 18°$.

this rapid change in curvature a flipping moment (concave to convex profile), in which the surface energy of dimples is converted into the kinetic energy, even though part of it dissipates through viscosity in the thin liquid film. To start the argument, we assume the surface energy of the interface before flipping can be defined as a $E_s \sim \sigma\pi(r_2^2 + L^2)$, in which r_2 is the size of the dimple before flipping and L is the height from the dimple to the center part of the thin film [the schematic is shown in Fig. 12(h)]. If we consider $L \sim h$, the surface energy can be rewritten as

$$E_s \sim \sigma\pi r_2^2[1 + (h/r_2)^2]. \tag{22}$$

To estimate the radius of the dimple, r_2, we balance two Young-Laplace pressure terms in Eq. (7); $\sigma/R \sim \sigma h/r_2^2$. The result will give a location where the pressure crosses zero, close to the radius of the dimple. Hence, we estimate the radius of the dimple as $\sqrt{Rh}$.

To approximate the viscosity effect inside a thin film, we define the dissipation energy as

$$E_d \sim \iint [\mu(\nabla u)^2]\, d\Omega_1\, dt \sim \mu(u/h)^2\pi(r_2)^2 h\Delta t, \tag{23}$$

where $\Omega_1 \sim \pi {r_2}^2 h$ is the volume of liquid inside the thin film. Here u is the parallel velocity, which can be approximated as $u \sim v r_2/2h$ using the mass balance and the normal velocity, v. Also, Δt is the timescale of the motion of the bubble surface, which scales as $\Delta t \sim 2L/v \sim 2h/v$. By

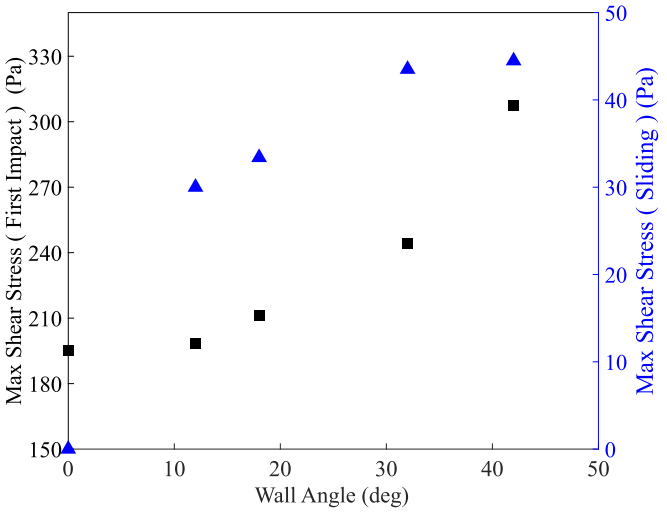

FIG. 14. Maximum shear stress generated during the first impact (■) and sliding stages (▲) for several wall angles.

considering these scalings, the dissipation energy becomes $E_d \sim \mu v\pi (r_2)^4/(2h^2)$. Here the net energy of $(E_s - E_d)$ will be transferred to the kinetic energy, $E_k \sim (1/2)\rho\Omega_2 v^2$. If we consider the volume of a displaced liquid during flipping as the volume of a spherical cap, $\Omega_2 \sim 2\{\frac{1}{6}\pi h {r_2}^2[3 + (h/r_2)^2]\}$, the energy balance of $(E_s - E_d = E_k)$ leads to following quadratic equation for v:

$$\frac{\rho}{6} v^2 h[3 + (h/r_2)^2] + \mu v (r_2)^2/(2h^2) = \sigma[1 + (h/r_2)^2]. \tag{24}$$

For a bubble impacting horizontal wall [Fig. 13(a)] by considering $r_2 \sim \sqrt{Rh}$, $u \sim v r_2/2h$, $R \approx 520\,\mu$m, and $h \approx 10\,\mu$m, the scaling for the generated shear stress is obtained by $\tau \sim \mu u/h \sim 730$ Pa, which is on the same order of magnitude as the shear stress in our simulation, ~200 Pa. However, the value is a bit higher than the simulation one. One reason for the difference is due to a

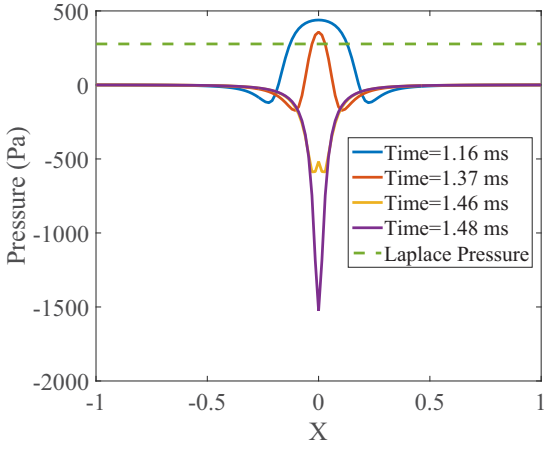

FIG. 15. Pressure profile inside liquid thin film as the bubble $R \approx 520\ \mu$m bounces away from the horizontal wall.

rough estimate of the dimple position of $r_2 \sim \sqrt{Rh}$ based on a very simple pressure balance between two terms in Eq. (7) (pressure profile inside thin film is shown in Fig. 15). It is worth noting that the shear stress profile for the later part of bubble motions in Fig. 13(a) is in good agreement with the previous study [79].

V. CONCLUSION AND DISCUSSION

In this study, we have investigated the dynamics of a rising bubble interacting with a wall and calculated the shear stress that can be generated during this process. As a bubble impacts a surface, a thin layer of fluid is formed between the bubble and the wall. Through the numerical model, we simulated a profile of the thin liquid film which can give us both pressure distribution inside the film and shear stress on the wall. Good agreement with experimental results has been obtained by considering the lift force and asymmetric thin film profile. We showed that during the bouncing stage, the generated shear stress inside the thin film can be up to the order of ∼307 Pa. Such a high shear stress has also been explained through the scaling law argument, in which a flipping dimple during the bouncing stage leads to a rapid change in the interfacial curvature (change from the concave to convex profile or flipping motion). Also, during the later sliding stage, the maximum shear stress on the order of ∼44.5 Pa has been calculated for a bubble moving along the wall with $\theta = 42^\circ$. It shows that the bubble-wall interaction has a potential for removing the biofilm.

Due to shear or capillary force, fluid flows could remove bacteria from various surfaces [45,48,80–85]. In practice, several parameters such as the type of bacteria and a surface, settling time, and washing time can change the criterion of detachment. For example, in the case of *E. coli* B/r cells, the critical shear stress of 0.03–5 Pa is needed to remove 99.5% of cells from the polymer-treated glass or 65% of cells from the control octadecyl glass [45]. For *Listeria monocytogenes*, the shear stress from 24 to 144 Pa is needed to eliminate bacteria from a stainless steel surface up to 98% [48]. In Fig. 16 we summarize the critical shear stress (more than 50% detachment) for five different types of bacteria to be compared with our simulation results for a bubble impacting a tilted wall of 42°. In general, the generated shear stress of about 300 Pa is enough to remove typical foodborne pathogens from surfaces.

It is worth noting that the applicability of our study with the assumption of clean bubbles. One concern might be liquid contamination in real produce cleaning applications, while our study is based on clean (mobile) bubbles for zero to low concentration of contamination. According to

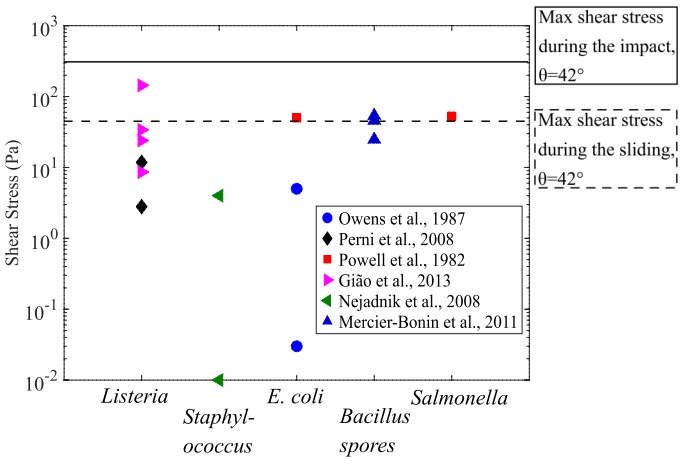

FIG. 16. Shear stress required to remove bacteria from a surface compared with the stress generated during the bubble impact at $\theta = 42^\circ$.

previous studies [86–88], there is a range of concentration in a bulk fluid below which a bubble interface can be considered as a mobile interface. The typical volume concentration of a bacterium culture ($V_{\text{Bacteria}}/V_{\text{Bulk}} \sim 1.96 \times 10^{-8}$) for foodborne disease studies based on real fruit biofilms [89] is less than the critical concentration to be a mobile interface reported in the previous studies [86–88]. In fact, even in our PIV test with micron-sized particles, we observed that the terminal rising velocity was about 26.14 ± 1.04 (cm/s), which is much closer to the value of a clean bubble rising velocity (29 cm/s [26]) as opposed to the value for contaminated bubble (around 10 cm/s [26]). Another concern is the surface curvature and length scale of real fruit cases. The surface curvature (inverse of length scale) is important only when the curvature is on the same order of magnitude with the inverse of a bubble-bouncing distance. For a target fruit like tomato, which is more than 5 cm in radius, radius of curvature is larger than the bouncing distance. So, even though our study is on a tilted surface with a fixed angle, the effect of the wall curvature is not important during a few bouncing motions. Therefore, we believe that our experimental and computational study presented here is applicable to a device of using bubbles to clean real agricultural produce.

ACKNOWLEDGMENT

This work was partially supported by the National Science Foundation (Grant No. CBET-1604424).

[1] T. Temesgen, T. T. Bui, M. Han, T.-il Kim, and H. Park, Micro and nanobubble technologies as a new horizon for water-treatment techniques: A review, Adv. Colloid Interface Sci. **246**, 40 (2017).
[2] Y. J. Chan, M. F. Chong, C. L. Law, and D. G. Hassell, A review on anaerobic—Aerobic treatment of industrial and municipal wastewater, Chem. Eng. J. **155**, 1 (2009).
[3] P. R. Gogate and A. B. Pandit, A review of imperative technologies for wastewater treatment I: Oxidation technologies at ambient conditions, Adv. Environ. Res. **8**, 501 (2004).
[4] G. W. Gale and A. A. Busnaina, Removal of particulate contaminants using ultrasonics and megasonics: A review, Part. Sci. Technol. **13**, 197 (1995).
[5] J. Durkee, *Management of Industrial Cleaning Technology and Processes* (Elsevier, Oxford, 2006).
[6] C. Gómez-Suárez, H. J. Busscher, and H. C. van der Mei, Analysis of bacterial detachment from substratum surfaces by the passage of air-liquid interfaces, Appl. Environ. Microbiol. **67**, 2531 (2001).
[7] P. K. Sharma, M. J. Gibcus, H. C. van der Mei, and H. J. Busscher, Influence of fluid shear and microbubbles on bacterial detachment from a surface, Appl. Environ. Microbiol. **71**, 3668 (2005).
[8] P. K. Sharma, M. J. Gibcus, H. C. Van Der Mei, and H. J. Busscher, Microbubble-induced detachment of coadhering oral bacteria from salivary pellicles, Eur. J. Oral Sci. **113**, 326 (2005).
[9] M. R. Parini and W. G. Pitt, Dynamic removal of oral biofilms by bubbles, Colloids Surf. B **52**, 39 (2006).
[10] M. Menesses, J. Belden, N. Dickenson, and J. Bird, Measuring a critical stress for continuous prevention of marine biofouling accumulation with aeration, Biofouling **33**, 703 (2017).
[11] E. Scallan, R. M. Hoekstra, F. J. Angulo, R. V. Tauxe, M.-A. Widdowson, S. L. Roy, J. L. Jones, and P. M. Griffin, Foodborne illness acquired in the United States—Major pathogens, Emerg. Infect. Dis. **17**, 7 (2011).
[12] E. Scallan, P. M. Griffin, F. J. Angulo, R. V. Tauxe, and R. M. Hoekstra, Foodborne illness acquired in the United States—Unspecified agents, Emerg. Infect. Dis. **17**, 16 (2011).
[13] J. G. Morris Jr., How safe is our food? Emerg. Infect. Dis. **17**, 126 (2011).
[14] S. Jung and J. Eifert, Cleaning fruits using micro-bubbles (2016), available at https://www.foodonline.com/doc/cleaning-fruits-using-micro-bubbles-0001
[15] K. P. Cantor, C. F. Lynch, M. E. Hildesheim, M. Dosemeci, J. Lubin, M. Alavanja, and G. Craun, Drinking water source and chlorination byproducts I. Risk of bladder cancer, Epidemiology **9**, 21 (1998).

[16] K. S. Crump and H. A. Guess, Drinking water and cancer: Review of recent epidemiological findings and assessment of risks, Annu. Rev. Public Health **3**, 339 (1982).
[17] W. K. Jo, C. P. Weisel, and P. J. Lioy, Chloroform exposure and the health risk associated with multiple uses of chlorinated tap water, Risk Anal. **10**, 581 (1990).
[18] B. Verhaagen and D. F. Rivas, Measuring cavitation and its cleaning effect, Ultrasonics Sonochem. **29**, 619 (2016).
[19] F. Reuter and R. Mettin, Mechanisms of single bubble cleaning, Ultrasonics Sonochem. **29**, 550 (2016).
[20] R. Clift, J. R. Grace, and M. E. Weber, *Bubbles, Drops, and Particles* (Courier Corporation, 2005).
[21] L. Amaya-Bower and T. Lee, Single bubble rising dynamics for moderate Reynolds number using lattice Boltzmann method, Comput. Fluids **39**, 1191 (2010).
[22] P. C. Duineveld, The rise velocity and shape of bubbles in pure water at high Reynolds number, J. Fluid Mech. **292**, 325 (1995).
[23] F. Peters and C. Els, An experimental study on slow and fast bubbles in tap water, Chem. Eng. Sci. **82**, 194 (2012).
[24] M. Wu and M. Gharib, Experimental studies on the shape and path of small air bubbles rising in clean water, Phys. Fluids **14**, L49 (2002).
[25] E. Pelletier, C. Béguin, and S. Étienne, Experiments of air bubbles impacting a rigid wall in tap water, Phys. Fluids **27**, 123302 (2015).
[26] R. Manica, E. Klaseboer, and D. Y. C. Chan, Force balance model for bubble rise, impact, and bounce from solid surfaces, Langmuir **31**, 6763 (2015).
[27] J. Zawala, "Immortal" liquid film formed by colliding bubble at oscillating solid substrates, Phys. Fluids **28**, 057103 (2016).
[28] J. Zawala, D. Kosior, T. Dabros, and K. Malysa, Influence of bubble surface fluidity on collision kinetics and attachment to hydrophobic solids, Colloids Surf. A **505**, 47 (2016).
[29] M. Krasowska and K. Malysa, Kinetics of bubble collision and attachment to hydrophobic solids: I. Effect of surface roughness, Intl. J. Miner. Process. **81**, 205 (2007).
[30] E. Klaseboer, R. Manica, M. H. W. Hendrix, C.-D. Ohl, and D. Y. C. Chan, A force balance model for the motion, impact, and bounce of bubbles, Phys. Fluids **26**, 092101 (2014).
[31] E. Klaseboer, J.-P. Chevaillier, A. Maté, O. Masbernat, and C. Gourdon, Model and experiments of a drop impinging on an immersed wall, Phys. Fluids **13**, 45 (2001).
[32] J. Zawala and K. Malysa, Influence of the impact velocity and size of the film formed on bubble coalescence time at water surface, Langmuir **27**, 2250 (2011).
[33] T. Maxworthy, Bubble rise under an inclined plate, J. Fluid Mech. **229**, 659 (1991).
[34] H.-K. Tsao and D. L. Koch, Observations of high Reynolds number bubbles interacting with a rigid wall, Phys. Fluids **9**, 44 (1997).
[35] B. Podvin, S. Khoja, F. Moraga, and D. Attinger, Model and experimental visualizations of the interaction of a bubble with an inclined wall, Chem. Eng. Sci. **63**, 1914 (2008).
[36] C. E. Norman and M. J. Miksis, Dynamics of a gas bubble rising in an inclined channel at finite Reynolds number, Phys. Fluids **17**, 022102 (2005).
[37] K. M. DeBisschop, M. J. Miksis, and D. M. Eckmann, Bubble rising in an inclined channel, Phys. Fluids **14**, 93 (2002).
[38] L. Zhu and F. Gallaire, A pancake droplet translating in a hele-shaw cell: lubrication film and flow field, J. Fluid Mech. **798**, 955 (2016).
[39] E. Reyssat, Drops and bubbles in wedges, J. Fluid Mech. **748**, 641 (2014).
[40] E. Klaseboer, R. Gupta, and R. Manica, An extended Bretherton model for long Taylor bubbles at moderate capillary numbers, Phys. Fluids **26**, 032107 (2014).
[41] P. Aussillous and D. Quéré, Bubbles creeping in a viscous liquid along a slightly inclined plane, Europhys. Lett. **59**, 370 (2002).
[42] C. Dubois, A. Duchesne, and H. Caps, Between inertia and viscous effects: Sliding bubbles beneath an inclined plane, Europhys. Lett. **115**, 44001 (2016).
[43] E. Sawaguchi, A. Matsuda, K. Hama, M. Saito, and Y. Tagawa, Droplet levitation over a moving wall with a steady air film, J. Fluid Mech. **862**, 261 (2019).

[44] N. P. Boks, W. Norde, H. C. van der Mei, and H. J. Busscher, Forces involved in bacterial adhesion to hydrophilic and hydrophobic surfaces, Microbiology **154**, 3122 (2008).
[45] N. F. Owens, D. Gingell, and P. R. Rutter, Inhibition of cell adhesion by a synthetic polymer adsorbed to glass shown under defined hydrodynamic stress, J. Cell Sci. **87**, 667 (1987).
[46] M. Mukumoto, T. Ohshima, M. Ozaki, H. Konishi, N. Maeda, and Y. Nakamura, Effect of microbubbled water on the removal of a biofilm attached to orthodontic appliances—An in vitro study, Dental Mater. J. **31**, 821 (2012).
[47] J. E. Duddridge, C. A. Kent, and J. F. Laws, Effect of surface shear stress on the attachment of *Pseudomonas fluorescens* to stainless steel under defined flow conditions, Biotechnol. Bioeng. **24**, 153 (1982).
[48] M. S. Gião and C. W. Keevil, Hydrodynamic shear stress to remove *Listeria monocytogenes* biofilms from stainless steel and polytetrafluoroethylene surfaces, J. Appl. Microbiol. **114**, 256 (2013).
[49] S. Khodaparast, M. K. Kim, J. E. Silpe, and H. A. Stone, Bubble-driven detachment of bacteria from confined microgeometries, Environ. Sci. Technol. **51**, 1340 (2017).
[50] C. A. Rodesney, B. Roman, N. Dhamani, B. J. Cooley, A. Touhami, and V. D. Gordon, Mechanosensing of shear by *Pseudomonas aeruginosa* leads to increased levels of the cyclic-di-GMP signal initiating biofilm development, Proc. Natl. Acad. Sci. USA **114**, 5906 (2017).
[51] R. O'Reilly Meehan, B. Donnelly, K. Nolan, T. Persoons, and D. B. Murray, Flow structures and dynamics in the wakes of sliding bubbles, Intl. J. Multiphase Flow **84**, 145 (2016).
[52] W. Thielicke and E. J. Stamhuis, PIVlab - Towards user-friendly, affordable and accurate digital particle image velocimetry in MATLAB, J. Open Res. Softw. **2**, e30 (2014).
[53] J. Magnaudet and I. Eames, The motion of high-Reynolds-number bubbles in inhomogeneous flows, Annu. Rev. Fluid Mech. **32**, 659 (2000).
[54] S.-M. Yang and L. G. Leal, A note on memory-integral contributions to the force on an accelerating spherical drop at low Reynolds number, Phys. Fluids A **3**, 1822 (1991).
[55] R. Mei, J. F. Klausner, and C. J. Lawrence, A note on the history force on a spherical bubble at finite Reynolds number, Phys. Fluids **6**, 418 (1994).
[56] R. Manica, E. Klaseboer, and D. Y. C. Chan, The hydrodynamics of bubble rise and impact with solid surfaces, Adv. Colloid Interface Sci. **235**, 214 (2016).
[57] F. Takemura, S. Takagi, J. Magnaudet, and Y. Matsumoto, Drag and lift forces on a bubble rising near a vertical wall in a viscous liquid, J. Fluid Mech. **461**, 277 (2002).
[58] F. Takemura and J. Magnaudet, The transverse force on clean and contaminated bubbles rising near a vertical wall at moderate Reynolds number, J. Fluid Mech. **495**, 235 (2003).
[59] C. W. M. Van der Geld, On the motion of a spherical bubble deforming near a plane wall, J. Eng. Math. **42**, 91 (2002).
[60] J. Masliyah, R. Jauhari, and M. Gray, Drag coefficients for air bubbles rising along an inclined surface, Chem. Eng. Sci. **49**, 1905 (1994).
[61] L. Zeng, S. Balachandar, and P. Fischer, Wall-induced forces on a rigid sphere at finite Reynolds number, J. Fluid Mech. **536**, 1 (2005).
[62] C. W. M. Van der Geld, H. Van Wingaarden, and B. A. Brand, Experiments on the effect of acceleration on the drag of tapwater bubbles, Exp. Fluids **31**, 708 (2001).
[63] R. Slavchov, B. Radoev, and K. W. Stöckelhuber, Equilibrium profile and rupture of wetting film on heterogeneous substrates, Colloids Surf. A **261**, 135 (2005).
[64] M. H. W. Hendrix, R. Manica, E. Klaseboer, D. Y. C. Chan, and C.-D. Ohl, Spatiotemporal Evolution of Thin Liquid Films During Impact of Water Bubbles on Glass on a Micrometer to Nanometer Scale, Phys. Rev. Lett. **108**, 247803 (2012).
[65] A. Oron, S. H. Davis, and S. G. Bankoff, Long-scale evolution of thin liquid films, Rev. Mod. Phys. **69**, 931 (1997).
[66] N. H. Hammoud, P. H. Trinh, P. D. Howell, and H. A. Stone, Influence of Van der waals forces on a bubble moving in a tube, Phys. Rev. Fluids **2**, 063601 (2017).
[67] H. Lamb, *Hydrodynamics* (Dover, New York, 1945).

[68] A. A. Kharlamov, Z. Chára, and P. Vlasák, Hydraulic formulae for the added masses of an impermeable sphere moving near a plane wall, J. Eng. Math. **62**, 161 (2008).
[69] D. Legendre and J. Magnaudet, The lift force on a spherical bubble in a viscous linear shear flow, J. Fluid Mech. **368**, 81 (1998).
[70] G. Sridhar and J. Katz, Drag and lift forces on microscopic bubbles entrained by a vortex, Phys. Fluids **7**, 389 (1995).
[71] A. Tomiyama, H. Tamai, I. Zun, and S. Hosokawa, Transverse migration of single bubbles in simple shear flows, Chem. Eng. Sci. **57**, 1849 (2002).
[72] R. Adoua, D. Legendre, and J. Magnaudet, Reversal of the lift force on an oblate bubble in a weakly viscous linear shear flow, J. Fluid Mech. **628**, 23 (2009).
[73] D. Y. C. Chan, E. Klaseboer, and R. Manica, Theory of non-equilibrium force measurements involving deformable drops and bubbles, Adv. Colloid Interface Sci. **165**, 70 (2011).
[74] K. Ellingsen and F. Risso, On the rise of an ellipsoidal bubble in water: oscillatory paths and liquid-induced velocity, J. Fluid Mech. **440**, 235 (2001).
[75] G. Mougin and J. Magnaudet, Path Instability of a Rising Bubble, Phys. Rev. Lett. **88**, 014502 (2001).
[76] D. Platikanov, Experimental investigation on the "dimpling" of thin liquid films, J. Phys. Chem. **68**, 3619 (1964).
[77] L. Pan, S. Jung, and R.-H. Yoon, Effect of hydrophobicity on the stability of the wetting films of water formed on gold surfaces, J. Colloid Interface Sci. **361**, 321 (2011).
[78] A. M. Gañán-Calvo, Revision of Bubble Bursting: Universal Scaling Laws of Top Jet Drop Size and Speed, Phys. Rev. Lett. **119**, 204502 (2017).
[79] R. Manica, M. H. W. Hendrix, R. Gupta, E. Klaseboer, C.-D. Ohl, and D. Y. C. Chan, Modelling bubble rise and interaction with a glass surface, Appl. Math. Model. **38**, 4249 (2014).
[80] S. Perni, E. S. Read, and G. Shama, Detachment of *Listeria innocua* and *Pantoea agglomerans* from cylinders of agar and potato tissue under conditions of Couette flow, J. Food Eng. **89**, 355 (2008).
[81] M. S. Powell and N. K. H. Slater, Removal rates of bacterial cells from glass surfaces by fluid shear, Biotechnol. Bioeng. **24**, 2527 (1982).
[82] M. R. Nejadnik, H. C. van der Mei, W. Norde, and H. J. Busscher, Bacterial adhesion and growth on a polymer brush-coating, Biomaterials **29**, 4117 (2008).
[83] M. Mercier-Bonin, A. Dehouche, J. Morchain, and P. Schmitz, Orientation and detachment dynamics of *Bacillus* spores from stainless steel under controlled shear flow: Modelling of the adhesion force, Intl. J. Food Microbiol. **146**, 182 (2011).
[84] S. Lecuyer, R. Rusconi, Y. Shen, A. Forsyth, H. Vlamakis, R. Kolter, and H. A. Stone, Shear stress increases the residence time of adhesion of *Pseudomonas aeruginosa*, Biophys. J. **100**, 341 (2011).
[85] T. Saur, E. Morin, F. Habouzit, N. Bernet, and R. Escudié, Impact of wall shear stress on initial bacterial adhesion in rotating annular reactor, PloS ONE **12**, e0172113 (2017).
[86] R. Bel Fdhila and P. C. Duineveld, The effect of surfactant on the rise of a spherical bubble at high Reynolds and Péclet numbers, Phys. Fluids **8**, 310 (1996).
[87] K. Malysa, M. Krasowska, and M. Krzan, Influence of surface active substances on bubble motion and collision with various interfaces, Adv. Colloid Interface Sci. **114–115**, 205 (2005).
[88] V. Ulaganathan, M. Krzan, M. Lotfi, S. S. Dukhin, V. I. Kovalchuk, A. Javadi, D. Z. Gunes, C. Gehin-Delval, K. Malysa, and R. Miller, Influence of β-lactoglobulin and its surfactant mixtures on velocity of the rising bubbles, Colloids Surf. A **460**, 361 (2014).
[89] J. J. Lee, J. D. Eifert, S. Jung, and L. K. Strawn, Cavitation bubbles remove and inactivate listeria and salmonella on the surface of fresh roma tomatoes and cantaloupes, Front. Sustain. Food Syst. **2**, 61 (2018).